The Astrophysical Journal, 976:11 (10pp), 2024 November 20 https://doi.org/10.3847/1538-4357/ad7c49

Reconstruction of the Total Solar Irradiance During the Last Millennium

Valentina Penza[1], Luca Bertello[2], Matteo Cantoresi[1], Serena Criscuoli[2], Lorenza Lucaferri[1], Raffaele Reda[1], Simone Ulzega[3], and Francesco Berrilli[1]
[1] Dipartimento di Fisica, Università degli Studi di Roma Tor Vergata, Via della Ricerca Scientifica 1, Roma, 00133, Italy; francesco.berrilli@roma2.infn.it
[2] National Solar Observatory, 3665 Discovery Dr., Boulder, CO 80303, USA
[3] Institute of Computational Life Sciences, Zurich University of Applied Sciences (ZHAW), 8820 Wädenswil, Switzerland
Received 2024 July 3; revised 2024 September 15; accepted 2024 September 16; published 2024 November 11

Abstract

Solar irradiance variations across various timescales, from minutes to centuries, represent a potential natural driver of past regional and global climate cold phases. To accurately assess the Sun's effect on climate, particularly during periods of exceptionally low solar activity, known as grand minima, an accurate reconstruction of solar forcing is essential. While direct measurements of the total solar irradiance (TSI) only began in the late 1970s, with the advent of space radiometers, indirect evidence from various historical proxies suggests that the Sun's magnetic activity has undergone possible significant fluctuations over much longer timescales. Employing diverse and independent methods for TSI reconstruction is essential to gaining a comprehensive understanding of this issue. This study employs a semi-empirical model to reconstruct TSI over the past millennium. Our approach uses an estimated open solar magnetic field (F_o), derived from cosmogenic isotope data, as a proxy for solar activity. We reconstruct the cyclic variations of TSI, due to the solar surface magnetic features, by correlating F_o with the parameter of active region functional form. We obtain the long-term TSI trend by applying the empirical mode decomposition algorithm to the reconstructed F_o to filter out the 11 yr and 22 yr solar variability. We prepare a reconstructed TSI record, spanning 971 to 2020 CE. The estimated departure from modern TSI values occurred during the Spörer minimum (around 1400 CE), with a decrease of approximately 2.3 Wm^{-2}. A slightly smaller decline of 2.2 Wm^{-2} is reported during the Maunder minimum, between 1645 and 1715 CE.

Unified Astronomy Thesaurus concepts: Solar physics (1476); Solar radiation (1521)

1. Introduction

Solar radiation is the most significant energy contributor to the Earth's energy budget (T. S. L'Ecuyer et al. 2015; A. C. Kren et al. 2017) and is a crucial external factor influencing the global climate (J. H. Jungclaus et al. 2017; Intergovernmental Panel on Climate Change (IPCC) 2023). Similarly, stellar irradiance and its variability affect the atmosphere of exoplanets and their habitability (e.g., J. L. Linsky 2017; D. Galuzzo et al. 2021; A. Modi et al. 2023) and affect our ability to detect exoplanets (e.g., D. Galuzzo et al. 2021; B. V. Rackham et al. 2023).

Total solar irradiance (TSI) is the amount of solar radiative energy integrated over the entire spectrum measured at a distance of 1 au. Prior to the space age, which enabled precise measurements of solar irradiance outside the Earth's atmosphere, TSI was considered unchanging over time, to the extent that it was defined as the solar constant. Highly accurate measurements from space commenced in the late 1970s and have allowed the assessment of TSI variations over timescales ranging from minutes to decades (e.g., P. Foukal & J. Lean 1988; J. Lean et al. 1995; S. K. Solanki & M. Fligge 1999; A. I. Shapiro et al. 2011; G. Kopp et al. 2016). In particular, the periodicity of TSI variations over the 11 yr solar cycle has been assessed. These variations, in phase with the solar cycle, can be quantified at approximately 0.1% from minimum to maximum (e.g., G. Kopp et al. 2016).

Although based on different methodologies, these models are predicated on empirical evidence that the TSI is modulated by photospheric magnetic field concentrations. Sunspots provide a negative contribution, while faculae and the network provide positive contributions (e.g., M. Steinegger et al. 1996; F. Berrilli et al. 1999; I. Ermolli et al. 2003). During the 11 yr cycle, the contribution from faculae exceeds that of sunspots, resulting in a positive correlation between TSI and other activity indices, such as for instance the sunspot number (SSN), at this temporal scale.

Space observations have only been gathering data for roughly 40 yr. Variations on centennial scales are clearly visible in the trend of the maxima of the SSN data set, which represents the direct solar observables covering the longest historical period (e.g., W. Gleissberg 1939; R. Arlt & J. M. Vaquero 2020 and references therein). In particular, the SSN observations over the past 400 yr have revealed the presence of periods of grand maxima and minima of solar activity (e.g., M. Stuiver & T. F. Braziunas 1998; M. Vonmoos et al. 2006; I. G. Usoskin et al. 2007; J. A. Abreu et al. 2008; A. Vecchio et al. 2017). Among the grand minima, the Maunder minimum, occurring in the latter half of the seventeenth century, stands out as the most widely studied. The estimates of irradiance variations from timescales of decades to millennia are an important input to global Earth climate models (see, e.g., M. Lockwood 2012; S. K. Solanki et al. 2013; I. Bordi et al. 2015; K. Matthes et al. 2017; H.-L. Liu et al. 2023). A variety of models have been proposed in the literature that aim at reproducing solar irradiance variability over different periods, ranging from months (e.g., R. C. Willson et al. 1981; L. Oster et al. 1982; S. Sofia et al. 1982; P. Foukal & J. Lean 1988) to years (e.g., V. Penza et al. 2003; K. L. Yeo et al. 2017a, 2017b; J. L. Lean et al. 2020) to centuries (e.g., D. G. Preminger & S. R. Walton 2006;

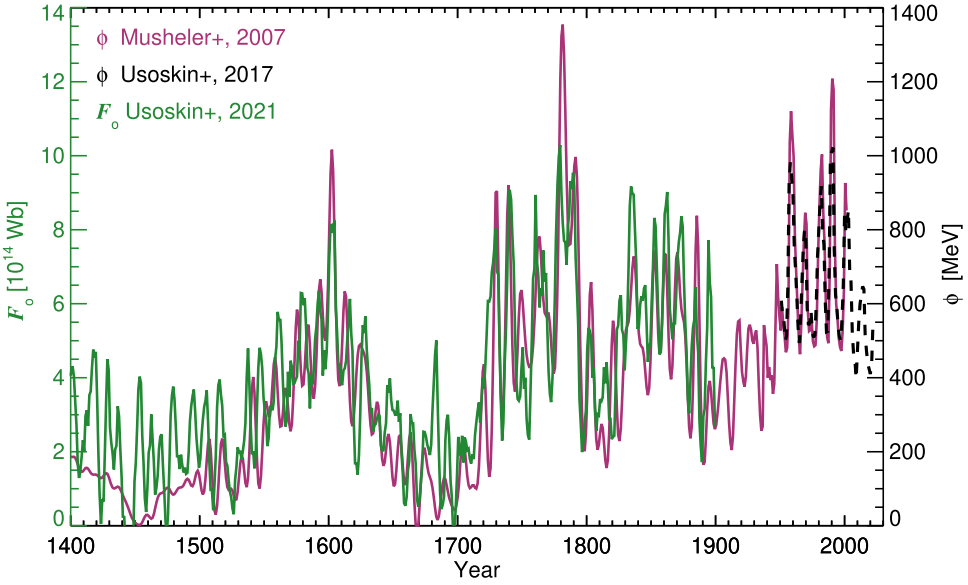

Figure 1. Comparison of the annual values of the open solar magnetic flux F_o, computed by I. G. Usoskin et al. (2021; green line), with the solar modulation potential ϕ values computed by R. Muscheler et al. (2007; purple line) and I. G. Usoskin et al. (2017; black dashed line).

K. F. Tapping et al. 2007; K. L. Yeo et al. 2014; O. Coddington et al. 2016; C.-J. Wu et al. 2018; V. Penza et al. 2022) and to millennia (e.g., J. L. Lean 2018; Y. Abduallah et al. 2021). Recent reviews of TSI reconstructions are provided in M. Faurobert (2019), G. Kopp & A. Shapiro (2021), G. Petrie et al. (2021), and T. Chatzistergos et al. (2023). Here, it is important to recognize that irradiance reconstructions before the twentieth century typically depend on proxies (SSN or sunspot groups and radioisotopes). Models vary, from using correlations between irradiance and proxies based on modern observations (F. Steinhilber et al. 2009; J. L. Lean 2018) to employing models of varying complexity to determine the distribution of magnetic fields across the solar disk (e.g., Y. M. Wang et al. 2005; C.-J. Wu et al. 2018).

This work is the natural continuation of the approach proposed in V. Penza et al. (2022). In that paper, the modulation on centennial timescales (from 1513 EC to the present) was derived from the decomposition of the solar modulation potential ϕ (R. Muscheler et al. 2016; N. Brehm et al. 2021) on different timescale components, derived with an empirical mode decomposition (EMD) algorithm.

The solar modulation potential ϕ represents the average energy loss of a cosmic ray from the heliopause to the Earth, due to the interaction with the heliosphere (see, e.g., L. J. Gleeson & W. I. Axford 1968; R. A. Caballero-Lopez & H. Moraal 2004). Because the interplanetary physical and magnetic conditions change with the level of solar magnetism, ϕ is a proxy of solar magnetic activity. The modulation potential is typically calculated using data from multiple neutron monitors (see, e.g., J. A. Simpson 2000), following a method initially proposed by I. G. Usoskin et al. (2005). For a detailed explanation, please refer to the paper by I. G. Usoskin et al. (2005).

In order to extend the TSI reconstruction backward by a thousand years and provide detailed information on individual cycles, we apply the same approach to the open solar magnetic field (F_o). F_o and ϕ are strongly correlated physical quantities, as the latter is a parameterization of the cosmic ray intensity, which is in turn modulated by the heliospheric magnetic field.

The relationship between the cosmic ray intensity and F_o has been investigated and established in several works (see, e.g., R. A. Caballero-Lopez & H. Moraal 2004; K. McCracken & J. Beer 2007), and in F. Steinhilber et al. (2010) an analytical power-law relationship between F_o and ϕ is derived. Here, we use the F_o data set reconstructed by I. G. Usoskin et al. (2021) with an annual cadence for the period 971–1899 EC, based on cosmic-ray flux data assessed from cosmogenic isotope ^{14}C measurements in tree rings (N. Brehm et al. 2021), and we extend this data set for the period 1900–2020 EC by using an empirical relation between F_o and ϕ, similar to that made in F. Steinhilber et al. (2009). Moreover, in order to estimate the 11 yr variations, we use updated composites of sunspot and plage area coverages (T. Chatzistergos et al. 2020; S. Mandal et al. 2020), which cover the temporal periods 1874–2023 EC and 1893–2023 EC, respectively.

The paper is organized as follows: in Section 2, we provide a description of the F_o data set; in Section 3, we describe the procedure used to extract the long-term modulation function; Section 4 describes the technique used to reconstruct the sunspot and plage coverages; the TSI reconstruction is shown and described in Section 5; and finally, in Section 6, we present a discussion of the results followed by a concise summary.

2. Open Solar Magnetic Flux Data Set

We use the data set of F_o as reconstructed by I. G. Usoskin et al. (2021).[4] This reconstruction contains data from 971 to 1899 CE with an annual cadence. In order to extend the data up to the present, we exploit a simple relation between the values of F_o and the values of the solar modulation potential ϕ (F_o and ϕ are shown in Figure 1). This relation is provided by the correlation between the values of F_o and ϕ by R. Muscheler et al. (2007) in the period 1513–1899 CE, which is shown in Figure 2. This specific time interval was chosen for comparison because, prior to this period, it is not possible to distinguish the 11 yr cycle variations in the ϕ data set. R. Muscheler et al. (2007) attribute this to the different time cadences in the ^{14}C

[4] http://cdsarc.u-strasbg.fr/viz-bin/cat?J/A+A/649/A141

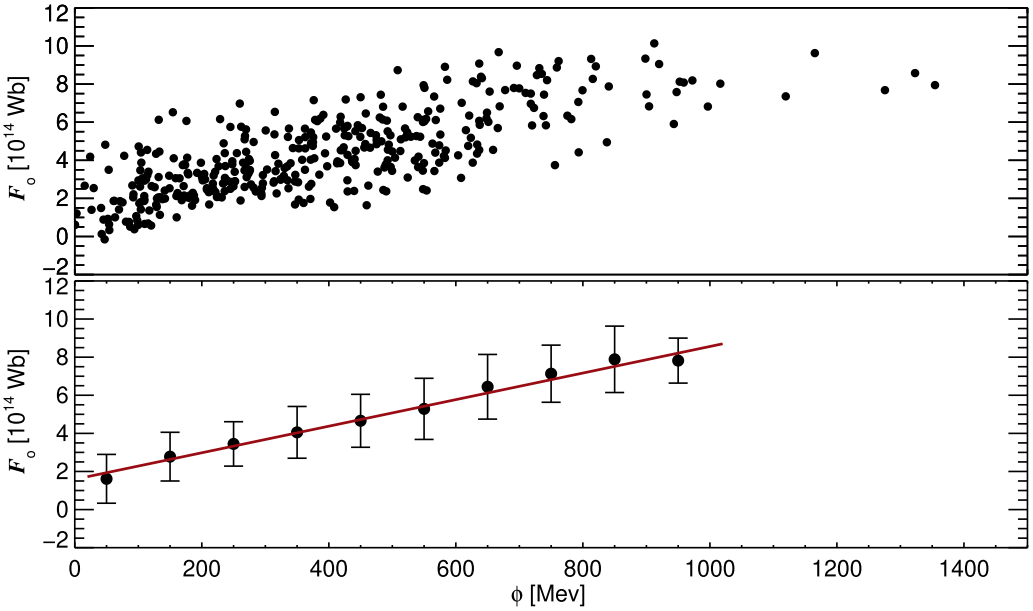

Figure 2. Top: the relationship between the annual values of the open solar magnetic flux F_o from I. G. Usoskin et al. (2021) and the solar modulation potential ϕ from R. Muscheler et al. (2007) for the years 1513–1899. Bottom: the same relationship after the data were divided into Gaussian bins with an FWHM of 100 Mev. The error bars represent the standard deviation of the weighted mean values. The red line represents the linear regression computed for ϕ value less than 1000 Mev (Equation (1) in the text). The Pearson's correlation coefficient is 0.996, statistically significant at $p < 0.01$

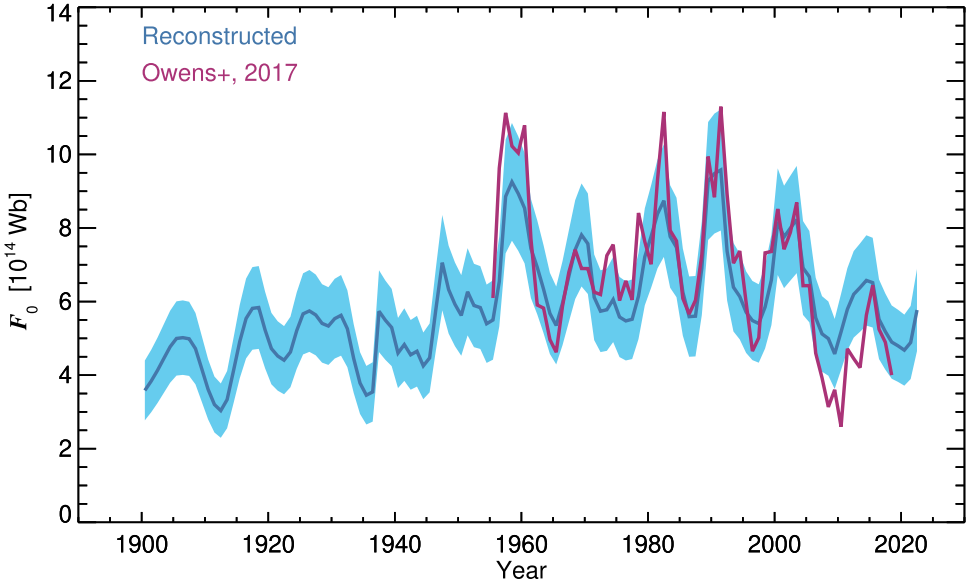

Figure 3. Reconstruction of the open solar magnetic flux F_o for the last century, depicted in blue. The light blue region illustrates the uncertainty range in the reconstructed time series. For comparison, data from M. J. Owens et al. (2017) spanning the time interval 1950–2022 are shown in red.

record. Furthermore, due to a limited number of points, the data above $\phi = 1000$ MeV may not be statistically significant. Therefore, we consider the parameters of a linear fit obtained for $\phi < 1000$ MeV. This choice is supported by the fact that for the period during which we will use this relation (after 1900 EC), the composite ϕ presents a maximum value of 1022 MeV, occurring in 1991 EC. The relation is the following:

$$F_o = (0.008 \pm 0.002)\,\phi + (1.4 \pm 0.9) \quad 10^{14}\text{Wb}. \qquad (1)$$

The Pearson's correlation coefficient for this relation is 0.996, statistically significant at $p < 0.01$.

We apply Equation (1) to the ϕ composite for the period 1513–2020 CE, obtained from the combination of two data sets: R. Muscheler et al. (2007) for 1900–1949 CE and I. G. Usoskin et al. (2017)[5] for 1950-2020 CE.

The F_o reconstruction for the post-1900 period, based on the linear relation provided above, is shown in Figure 3, where the observational data of M. J. Owens et al. (2017) are reported for comparison. The confidence interval is computed by propagation of the errors in the fit coefficients in Equation (1). We note that the reconstruction is compatible with experimental data within the error bars for almost all the years, except for a slight overestimation for the years between 2008 and 2014, corresponding to the minimum between Cycles 23 and 24.

[5] https://cosmicrays.oulu.fi/phi/phi.html

M. J. Owens et al. (2017) highlighted possible uncertainties in their data set during periods of minimal activity.

We use the composite of F_o both to reconstruct active region coverage and to obtain a long-term modulation function ($F_{\rm LT}(t)$), which is not present in the sunspot signal, to be applied to reconstruct the quiet network component. The latter is computed using a method similar to the one proposed in V. Penza et al. (2022): we decompose F_o by employing the EMD; we consider the intrinsic mode functions (IMFs) corresponding to the components not present in sunspots and the monotonic residual signal; and finally we properly standardize the data.

3. EMD and Hilbert Spectral Analysis

EMD (N. E. Huang et al. 1998) is a data-driven decomposition technique tailored to nonlinear and nonstationary signals, which makes possible the capturing of oscillatory modes with variable frequencies, enabling the examination of signal components across different scales. This outstanding feature of EMD has made it a widely used technique in several fields of physics, such as space and solar physics. In particular, within the latter, it has been used to study both short-term (D. Y. Kolotkov et al. 2015a) and long-term periodicities of solar activity (Q. Li et al. 2007; A. Vecchio et al. 2019), to extract the space climate variability in solar UV emission (M. Lovric et al. 2017) and solar wind properties (R. Reda et al. 2024), to reveal the presence of quasiperiodic pulsations in solar flares (V. M. Nakariakov et al. 2010; D. Y. Kolotkov et al. 2015b), as well as to identify the propagation of waves in the solar atmosphere (J. Terradas et al. 2004; M. Stangalini et al. 2014; S. M. Jefferies et al. 2019). One of its key features is that the decomposition basis is not prescribed a priori, in contrast to methods like Fourier analysis, which relies on a sinusoidal basis, or wavelet analysis, which utilizes a predefined mother wavelet. Indeed, EMD's strength lies in the adaptability of the decomposition basis, which is simply derived from the inherent properties of the signal under analysis via an iterative procedure known as the sifting process (see, e.g., G. Rilling et al. 2003). This procedure, which is based on interpolation by means of cubic splines, is such that each of the extracted modes have a zero-average mean envelope. The output of the sifting process is a set of IMFs, each one representing a mode of oscillation embedded in the starting signal. To be defined as such, an IMF must have the same number of extrema and zero crossings or differ by at most one. Overall, EMD enables the expression of any generic time series $s(t)$ as a finite sum of n time-dependent modes of oscillation (i.e., the IMFs) plus a residual term $R(t)$ that captures the time trend of the signal:

$$s(t) = \sum_{j=1}^{n} \mathrm{IMFj}_j(t) + R(t). \tag{2}$$

As previously mentioned, each IMF represents a proper mode of oscillation of the signal on a particular characteristic timescale. The EMD approach applied to the reconstruction of F_o results in seven IMFs and a monotonic residual, which are shown in the subplots of Figure 4. The corresponding characteristic timescales, as derived via Hilbert Spectral Analysis, are: $\tau_1 \simeq 3.6$ yr; $\tau_2 \simeq 10.5$ yr; $\tau_3 \simeq 21.6$ yr; $\tau_4 \simeq 45$ yr; $\tau_5 \simeq 115$ yr; $\tau_6 \simeq 211$ yr; and $\tau_7 \simeq 860$ yr. The estimation of the characteristic scale allows us to associate the majority of the components with known periodicities of solar activity. The first component (IMF 1) likely corresponds to quasi-biennial oscillations that are associated with the Gnevyshev gap (e.g., M. N. Gnevyshev 1967), which in turn is responsible for the double peak of the solar cycle (see, e.g., G. Bazilevskaya et al. 2014); IMF 2 and the IMF 3 are clearly associated with the Schwabe cycle (e.g., H. Schwabe & H. Schwabe 1844) and the Hale cycle (e.g., G. E. Hale et al. 1919), with IMF 3 possibly also reflecting a contribution from the Gnevyshev–Ohl rule (M. Gnevyshev & A. Ohl 1948); the fourth component (IMF 4) may represent a harmonic of the Hale cycle; IMF 5 shows a periodicity associated with the Gleissberg cycle (e.g., W. Gleissberg 1939); IMF 6 has a timescale compatible with the Suess–de Vries cycle (e.g., H. E. Suess 1980); and finally, the last component (IMF 7) may be linked to a lesser-known periodicity known as the Eddy cycle (e.g., F. Steinhilber et al. 2012; I. G. Usoskin 2017). At this stage, since our aim is to extract only the long-term modulation from F_o, we filter out the contribution of the components with $\tau \lesssim 22$ yr (i.e., IMF 1, IMF 2, and IMF 3). The resulting signal, later standardized, is shown in the bottom right subplot of Figure 4. Such a signal, namely $F_{\rm LT}$, constitutes the long-term modulation in the subsequent reconstructions.

The long-term modulation derived from F_o is utilized to reconstruct the impact of the magnetic fields of the quiet Sun on TSI variability. In the subsequent section, we will delve into an exploration of the contribution of magnetic fields from active regions, such as sunspots and faculae, to the TSI.

4. Plage and Sunspot Coverage Reconstruction

The irradiance variation on shorter timescales, up to a decade, are mainly modulated by the presence of bright and dark magnetic regions and by the disk surface fraction covered by them. In order to reconstruct this component, we use the same approach as in V. Penza et al. (2021, 2022). We utilize the functional form presented in D. Volobuev (2009) to mathematically represent individual sunspot cycles:

$$x_k(t) = \left(\frac{t - T0_k}{Ts_k}\right)^2 \exp\left[-\left(\frac{t - T0_k}{Td_k}\right)^2\right] \times T0_k < t < T0_k + \tau_k, \tag{3}$$

with $\mathrm{T0}_k$ and τ_k denoting the start year and duration of cycle k, respectively, and $x_k(t)$ referring to a solar activity proxy, such as sunspot area coverage or plage area coverage. The free parameters Td_k and Ts_k, both measured in years, characterize the overall shape of cycle k. Within the time interval of cycle k, the function $x_k(t)$ reaches its maximum, $(Td_k/Ts_k)^2 \exp(-1)$, at the time $t = T0_k + Td_K$. We define the parameter P_k as the ratio $(Td_k/Ts_k)^2$, which serves as an indicator of the peak intensity for cycle k.

The relationship between Ts_k and Td_k is known: cycles with large amplitude (smaller Ts_k) present a shorter time of rising to maximum (shorter Td_k). This is known as the Waldmeier rule.

As the data set of the sunspot area coverage (S. Mandal et al. 2020) is the same as in V. Penza et al. (2022), we use here the same Td_k and Ts_k (given in units of years) with their mutual relation:

$$Td_k^{\rm spot} = s_1 Ts_k^{\rm spot} + s_2, \tag{4}$$

where $s_1 = 0.02 \pm 0.01$ and $s_2 = 3.14 \pm 0.43$.

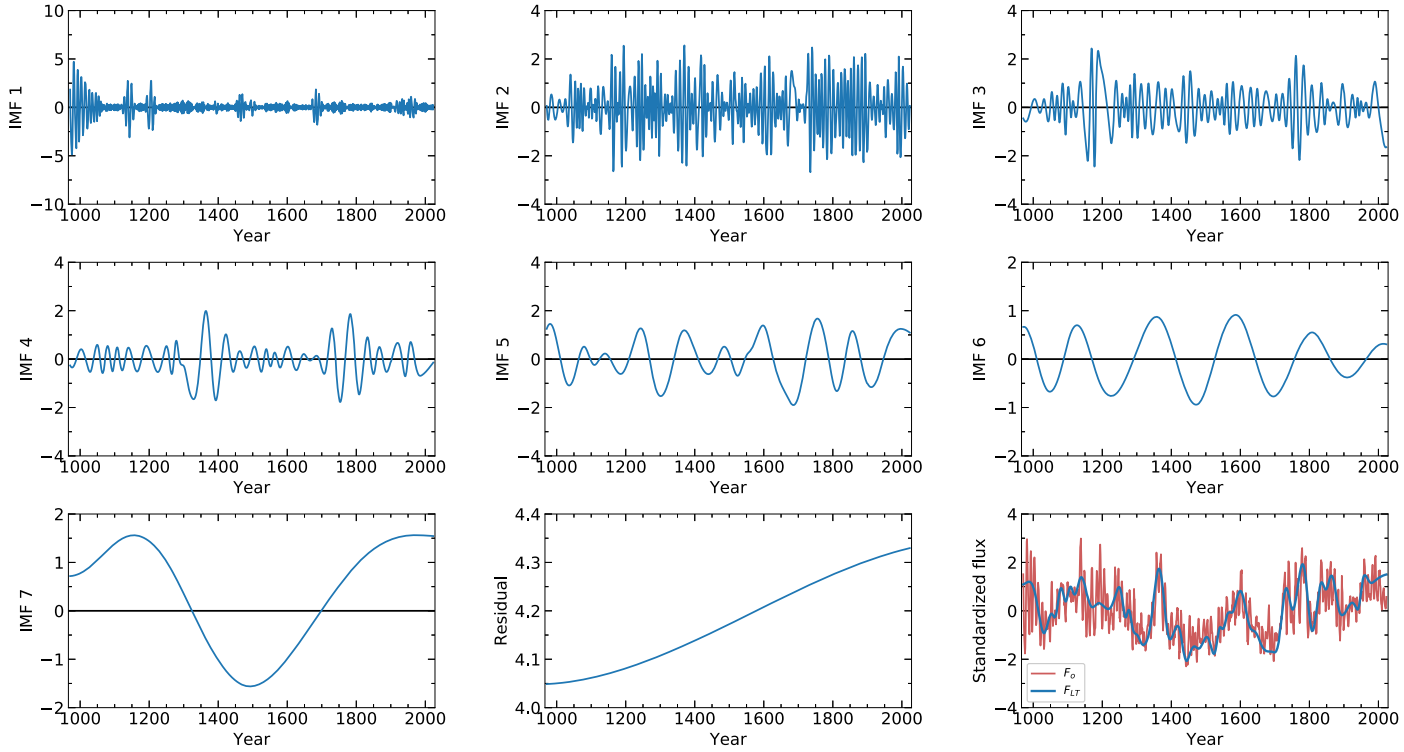

Figure 4. The IMFs extracted with EMD applied to the reconstruction of F_o. The panels in the first two rows, together with the leftmost panel in the third row, show the successive order IMFs. The center panel in the third row shows the residual signal of the decomposition. The modulation function ($F_{\rm LT}$), resulting from the standardized sum of IMFs 4–7 and the residual, is shown in the bottom right panel, along with the standardized F_o.

For the analysis of the plage area coverage, we use the recent data set published by T. Chatzistergos et al. (2020), which exhibits an increase in coverage levels during most minima compared to the data set used in a previous reconstruction (T. Chatzistergos et al. 2019). Since the functional form in Equation (3) is by definition zero when $t = T0$, we prefer to use a power-law relationship between plage areas and sunspots, as suggested in several studies (see, e.g., G. A. Chapman et al. 1997, 2011; T. Chatzistergos et al. 2022). We use two data sets of sunspot and plage area coverage within the common time range of 1903–2023 CE, and we consider their monthly average. As suggested in T. Chatzistergos et al. (2022), we find that the plage (α_f) and the sunspot (α_s) areas are linked by a power-law relationship (see Figure 5); in particular, we find the following best fit:

$$\alpha_f = (1.3 \pm 0.1)\alpha_s^{(0.61\pm0.02)} + (0.0042 \pm 0.0005). \quad (5)$$

We note that the parameters in Equation (5) are different from those reported in T. Chatzistergos et al. (2022). This is likely due to the use of monthly average values in our study instead of daily values. We report that the Spearman's rank correlation coefficient between sunspot and plage areas is 0.930, statistically significant at $p < 0.01$.

Following the approach described in V. Penza et al. (2022), we investigate the correlation between the parameters in Equation (3) and the cycle-averaged F_o values. The values of F_o are given with a yearly cadence and a substantial σ error (20%–40%), so we compute the average values through a Monte Carlo simulation of 1,000 iterations, where we calculate the average value over 11 yr, varying the F_o values within 3σ. Then, we consider the mean of the averages with the corresponding error given by the standard deviation. Given the high positive correlation between the 11 yr averaged values of F_o ($\overline{F_o}$) and of the sunspot area coverage, guaranteed by a Pearson's correlation coefficient $r = 0.81$, with a confidence level greater than 95% ($p = 0.048$), we search for a correlation between $\overline{F_o}$ and the parameter P_k:

$$P_k = a\overline{F_o} + b. \quad (6)$$

This is because we observe that the integral of the expression in Equation (3) over the cycle duration corresponds to the following expression:

$$\frac{\int_0^{\tau_k} x_k(t)dt}{\tau_k} = \left(\frac{Td_k}{2Ts_k}\right)^2 \times \left[\sqrt{\pi}\frac{\mathrm{erf}(f_k)}{f_k} - 2e^{-f_k^2}\right], \quad (7)$$

where $f_k \equiv \tau_k/Td_k$ and erf is the so-called error function. From the latter expression, it follows that the average coverage is proportional to the parameter P_k. On the other hand, we have verified that the term $\left[\sqrt{\pi}\frac{\mathrm{erf}(f_k)}{f_k} - 2e^{-f_k^2}\right]$ in Equation (7) does not correlate with $\overline{F_o}$.

By the best fit of Equation (6) (Figure 6), we obtain the following values:

$$a = 0.002 \pm 0.001 \ (\mathrm{Wb}^{-1})$$
$$b = -0.004 \pm 0.003. \quad (8)$$

Then we are able to obtain the values of the P_k parameter for all of the past cycles, from 971 to 1900 CE. The P_k values are obtained by the application of this relation. We are now able to calculate the individual parameters Ts_k and Td_k from P_k by using the relation provided in Equation (4). Subsequently, we

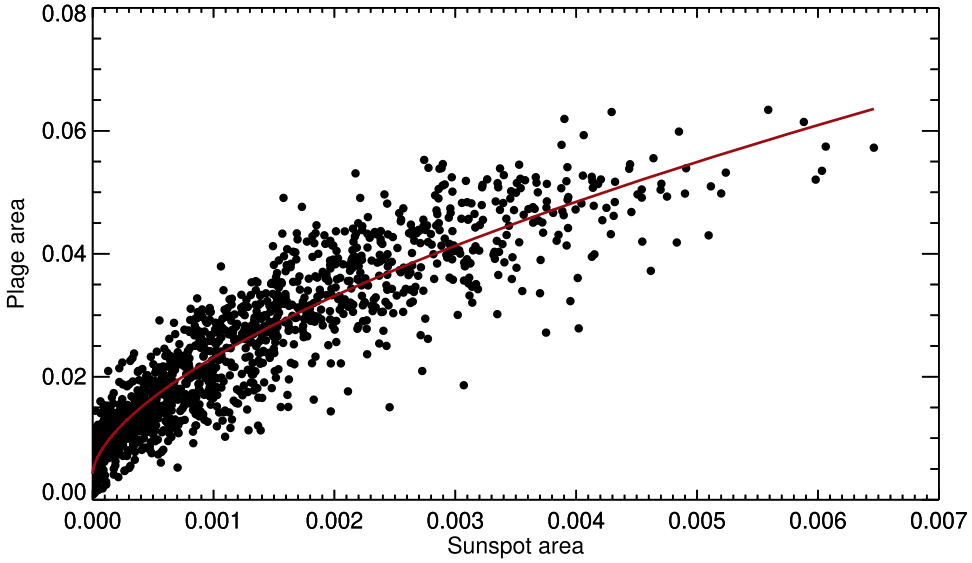

Figure 5. Relationship between monthly plage and sunspot area coverage for the years 1903–2023. The red curve represents the power-law fit to the data (Equation (5) in the text). The Spearman's rank correlation coefficient is 0.930, statistically significant at $p < 0.01$.

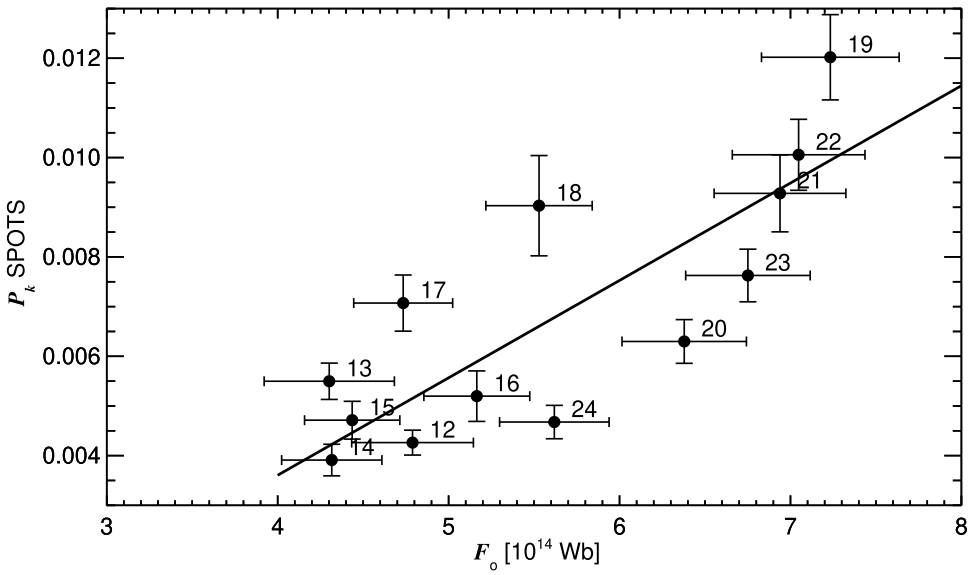

Figure 6. Dependence of the spot parameter P_k on the k-cycle-averaged open solar magnetic flux F_o. The individual solar cycle numbers are indicated in the plot, with error bars representing the 1σ standard error of the mean. This relationship is well described by the linear model (solid line) provided in Equation (6). The Pearson's correlation coefficient is 0.80, with a confidence level greater than 95% ($p = 0.048$).

reconstruct the sunspot coverage trend (Figure 7) by substituting these values into Equation (3). Finally, the plage coverage is reconstructed using the relationship described in Equation (5). The resulting reconstructed plage area is shown in Figure 8, together with the measured composite by T. Chatzistergos et al. (2020).

5. TSI Reconstruction

Solar irradiance variations can be accurately reproduced using a widely accepted method (e.g., V. Penza et al. 2003; I. Ermolli et al. 2011; J. M. Fontenla et al. 2011; W. T. Ball et al. 2014; S. Criscuoli et al. 2018; F. Berrilli et al. 2020). This method involves summing the fluxes generated by various solar components, each weighted according to its corresponding coverage area:

$$F(t) = \sum_j \alpha_j(t) F_j, \tag{9}$$

where F_j is the integral over all wavelengths of the spectrum of the flux from the j-feature (quiet, network, facula, and sunspot) —supposed to be time-independent—and $\alpha_j(t)$ is the respective coverage. In order to reconstruct the TSI variations, we proceed in the same way as in V. Penza et al. (2022), computing the TSI variations as:

$$\begin{aligned} F(t) = {} & \alpha_f(t)F_f + \alpha_n(t)F_n + \alpha_s(t)F_s \\ & + (1 - \alpha_f(t) - \alpha_n(t) + \alpha_s(t))F_q, \end{aligned} \tag{10}$$

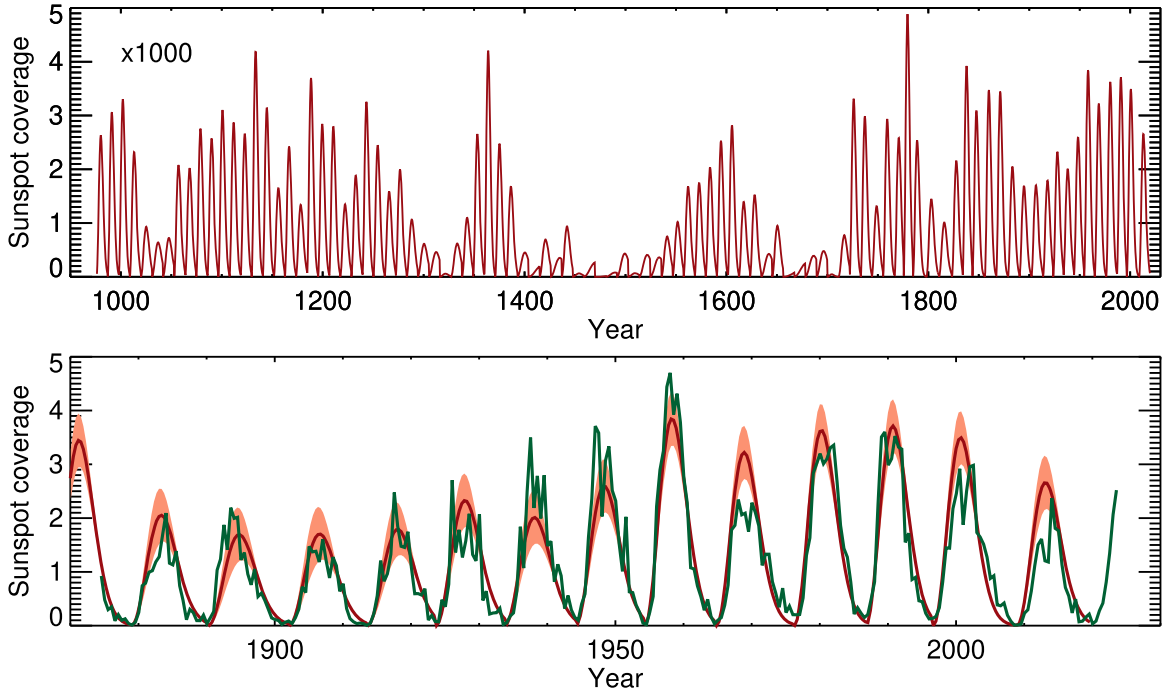

Figure 7. Top: reconstruction of sunspot area coverage from 971 CE to the present. Bottom: the reconstructed time series (red curve) and its uncertainty range (light red region) are shown from 1900 to the present. The actual measured monthly sunspot area coverage by S. Mandal et al. (2020) is shown in green.

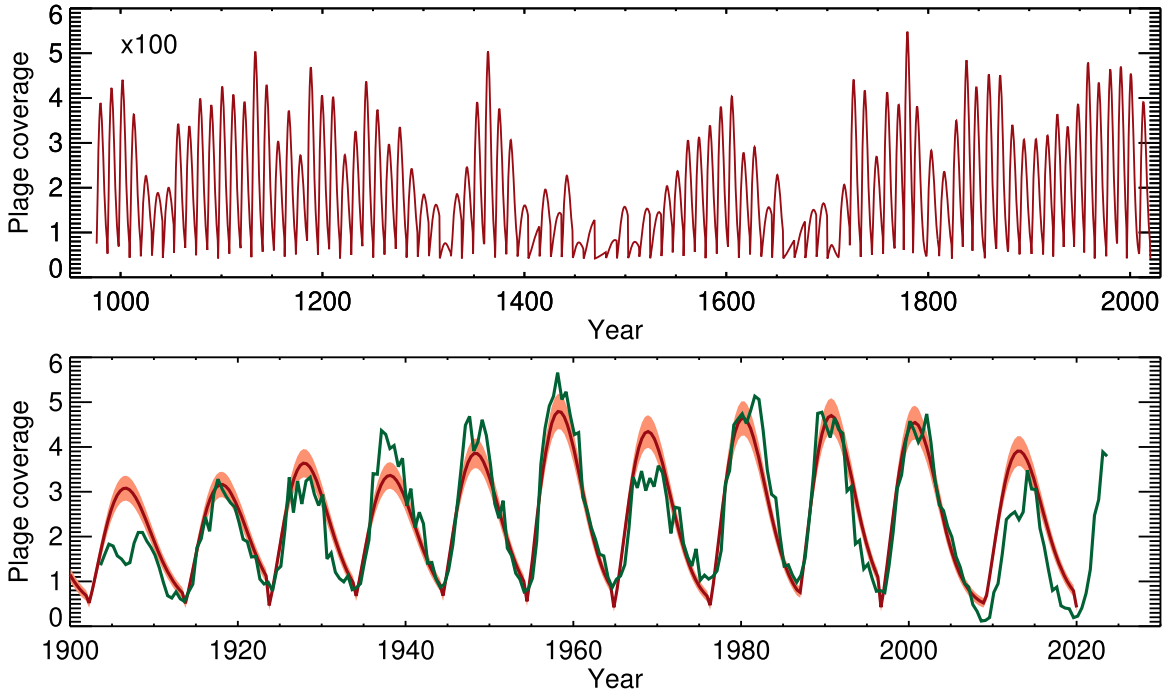

Figure 8. The same as Figure 7, but for the plage area coverage. The plage area composite by T. Chatzistergos et al. (2020) is shown in green.

where the subscripts f, n, s, and q indicate facular, network, sunspot, and solar quiet contributions, respectively. Then, the relative variation has a very simple form:

$$\delta F(t) \equiv \frac{F(t) - F_q}{F_q} = \alpha_f(t)\frac{F_f - F_q}{F_q} + \alpha_n(t)\frac{F_n - F_q}{F_q} + \alpha_s(t)\frac{F_s - F_q}{F_q} = \alpha_f(t)\delta_f + \alpha_n(t)\delta_n + \alpha_s(t)\delta_s, \quad (11)$$

where δ_f, δ_n, and δ_s are the relative contrasts.

We adopt a linear relation between $\alpha_f(t)$ and $\alpha_n(t)$ (see, e.g., S. Criscuoli et al. 2018; P. Devil et al. 2021). As inferred by A. Skumanich et al. (1984), this relationship is the consequence of the presumed derivation of the network components from the decay of the plage regions (see Figure 7 of A. Skumanich et al. 1984). By imposing the following relation,

$$\alpha_n = A_n + B_n\alpha_f(t), \quad (12)$$

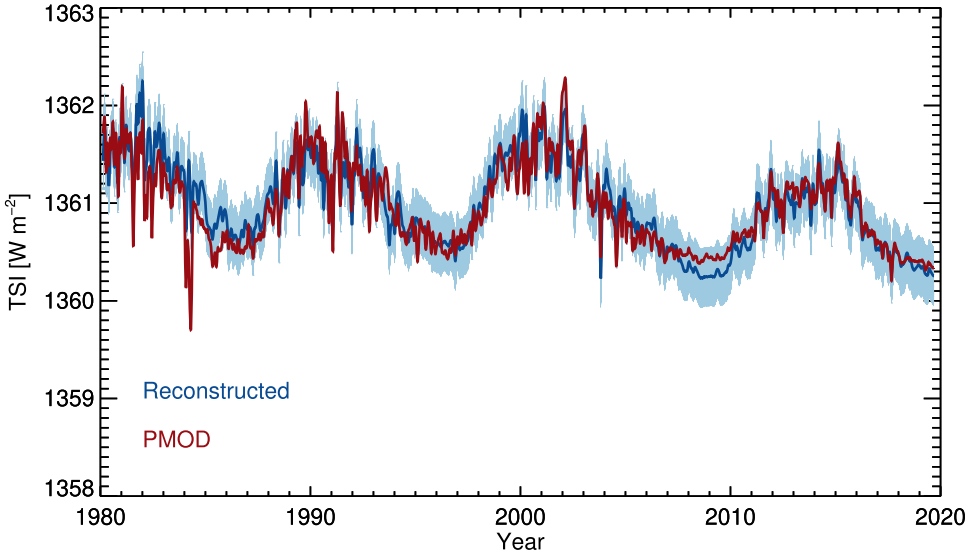

Figure 9. Comparison between the TSI–PMOD composite (red) and the reconstructed TSI time series (blue) from 1980 to 2020 CE (Equation (13)). The light blue region represents the uncertainty range in the reconstructed time series.

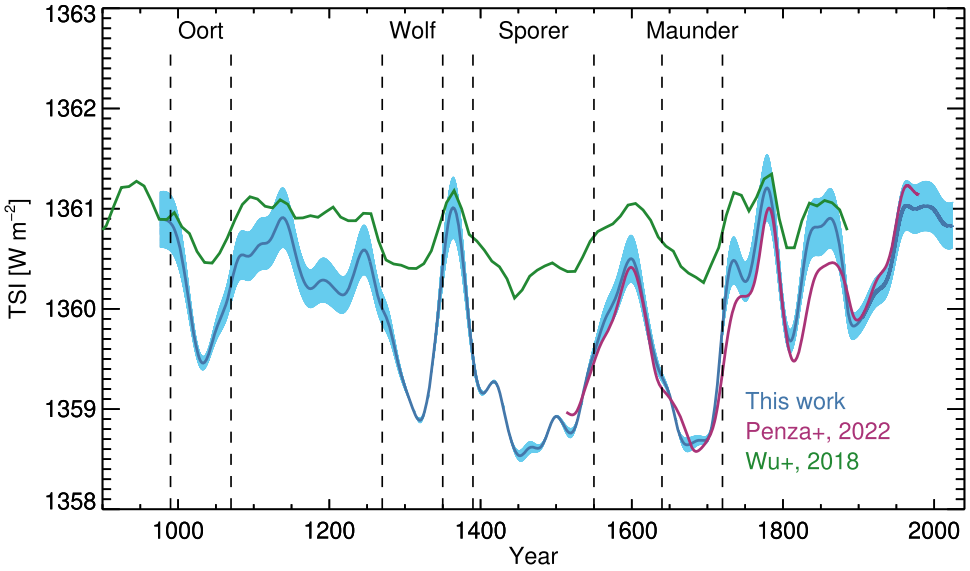

Figure 10. Three different TSI reconstructions are shown for comparison. The blue line, covering the period from 971 to 2020 CE, along with its uncertainty range (light blue region), represent the results from this work. The TSI values from C.-J. Wu et al. (2018) are depicted in green, while the purple line shows the reconstruction from our 2022 study (V. Penza et al. 2022).

we can rewrite Equation (11) as

$$\delta F(t) = Cn + \alpha_f(t)\delta_{fn} + \alpha_s(t)\delta_s, \quad (13)$$

where $\delta_{fn} \equiv \delta_f + B_n\delta_n$ is the mixed facular and network contribution, while $C_n \equiv A_n\delta_n$ represents the value of the network contrast weighted by the corresponding fractional area at the solar minimum.

The parameters C_n, δ_{fn}, and δs are obtained by fitting single cycles (Figure 9), where we can neglect the long-term modulation, with the PMOD–TSI composite[6] (J. Montillet et al. 2022). The values are slightly different with respect to V. Penza et al. (2022), as we have used a different plage coverage data set and now we are fitting over three complete solar cycles (22, 23, and 24):

$$\delta_{fn} = 0.041 \pm 0.002$$
$$\delta_s = -0.30 \pm 0.01$$
$$C_n = 8.8{\cdot}10^{-4} \pm 1{\cdot}10^{-4}.$$

Finally, we introduce a long-term modulation of the C_n values:

$$\delta F(t) = C_n[1 + F_{\rm LT}(t)]N_{\rm norm} + \alpha_f(t)\delta_{fn} + \alpha_s(t)\delta_s, \quad (14)$$

where $F_{\rm LT}(t)$ is the normalized long-term modulation function computed in Section 3 and $N_{\rm norm}$ is a normalization parameter. We employ two free parameters, $N_{\rm norm}$ and F_q, for the final reconstruction of $F(t)$ (Equation (10)). The best fit over the whole PMOD composite gives the values $N_{\rm norm} = 0.55$ and

[6] ftp.pmodwrc.ch/pub/data/irradiance/virgo/TSI/ (last accessed 2023 January).

$F_q = 1359.83\ \mathrm{Wm}^{-2}$, respectively. The result is shown in Figure 10, where, for comparison, the reconstructions by V. Penza et al. (2022) and that of C.-J. Wu et al. (2018) are included, with the latter only extending up to 1900 CE.

6. Discussion and Conclusions

In this work, we present a reconstruction of TSI variability over the last millennium, spanning from 971 to 2020 CE. This reconstruction builds upon the methodology proposed in our previous study (V. Penza et al. 2022), where the solar modulation potential (ϕ) was used as the principal proxy for TSI variability. In the current study, we employ the open solar magnetic field (F_o) as the main proxy, allowing us to extend the reconstruction farther back in time. Additionally, this reconstruction incorporates updated values of plage coverage (T. Chatzistergos et al. 2022) and TSI composites (J. Montillet et al. 2022).

Our approach integrates modern TSI measurements to estimate the contributions of sunspots and faculae in terms of their area coverages and bolometric contrasts. The resulting values for the bolometric contrasts reported in Section 5 agree remarkably well with those reported in the literature (e.g., G. A. Chapman et al. 1994; S. R. Walton et al. 2003; P. Foukal et al. 2004). A third, long-term component of our model takes into account weak magnetic features not associated with active regions (e.g., S. Marchenko et al. 2022) that modulate irradiance during minima. This third component is estimated from the low-frequency terms obtained from EMD applied to F_o and modern TSI measurements.

Our reconstruction (Figure 10) reveals four significant periods of grand minima, including the Spörer and Maunder minima. The Spörer minimum, occurring between the fifteenth and sixteenth centuries, shows a TSI variation of approximately $2.3\ \mathrm{Wm}^{-2}$ relative to present values, making it the deepest and longest minimum identified. We also estimate a growth in the TSI value of about $1\ \mathrm{Wm}^{-2}$ during the first half of the last century. After the 1960s, this value has remained substantially constant (on average) until the beginning of this century. The Maunder minimum shows a variation of $2.2\ \mathrm{Wm}^{-2}$ with respect to modern minima, which is very close to the value of $2.5\ \mathrm{Wm}^{-2}$ obtained in V. Penza et al. (2022). The use of F_o instead of ϕ, the different plage coverages and TSI composites, and the determination of the F_q parameter by fit are the main differences between the reconstructions presented in this study and our previous work.

The TSI variation between the Maunder minimum and the present found in our studies is higher than the values recently proposed in the literature. For instance, SATIRE produces a $0.55\ \mathrm{Wm}^{-2}$ variation (C.-J. Wu et al. 2018), in line with the more recent estimate of $0.5\ \mathrm{Wm}^{-2}$ by T. Chatzistergos et al. (2024). The model by Y. M. Wang & J. L. Lean (2021) produces a $0.2\ \mathrm{Wm}^{-2}$ variation. On the other hand, T. Egorova et al. (2018) obtained a TSI change between 3.7 and $4.5\ \mathrm{Wm}^{-2}$.

M. Lockwood & W. T. Ball (2020) placed a limit between 0.07 and $-0.13\ \mathrm{Wm}^{-2}$, indicating that within the constraints imposed by modern measurements, the TSI during grand minima could have been even higher than during current minima.

Our TSI reconstruction, and its reliability, depend on the composite of direct TSI measurements used (PMOD) and the choice to use cosmogenic data as a proxy for long-term variations. On the other hand, all the past reconstructions presented in the literature are based on similar assumptions and are prone to uncertainties propagating from the observational data and data products they rely on (e.g., T. Egorova et al. 2018; M. Lockwood & W. T. Ball 2020; T. Chatzistergos et al. 2023). Even models that try to tackle the issue from a different point of view, using 3D magnetohydrodynamic (MHD) simulations (K. L. Yeo et al. 2020; T. Chatzistergos et al. 2023), are inevitably bound by other assumptions, such as the small-scale dynamo not being affected by long-term variations. Despite the different approach, our result is compatible with the upper limit for TSI variations from the Maunder minimum to the present (about $2\ \mathrm{Wm}^{-2}$) estimated using MHD simulations by K. L. Yeo et al. (2020).

Acknowledgments

The National Solar Observatory is operated by the Association of Universities for Research in Astronomy, Inc. (AURA), under cooperative agreement with the National Science Foundation. L.B. and S.C. are members of the international team for Reconstructing Solar and Heliospheric Magnetic Field Evolution Over the Past Century, supported by the International Space Science Institute (ISSI), Bern, Switzerland. This research was partially supported by the Italian MIUR-PRIN Circumterrestrial Environment: Impact of Sun–Earth Interaction grant 2017APKP7T. M.C. and L.L. are supported by the Joint Research PhD Program in "Astronomy, Astrophysics and Space Science" between the University of Rome "Tor Vergata," the University of Rome "La Sapienza," and INAF. This research was part of the CAESAR (Comprehensive spAce wEather Studies for the ASPIS prototype Realization) project, supported by the Italian Space Agency and the National Institute of Astrophysics, through the ASI-INAF n.2020-35-HH.0 agreement for the development of the ASPIS (ASI SPace weather InfraStructure) prototype of a scientific data center for Space Weather.

The authors gratefully thank the anonymous referee for helpful comments and suggestions, Ilya Usoskin for providing the F_o data, Jürg Beer for useful information about the cosmogenic isotope measurements, and Valerio Formato for helpful discussions.

ORCID iDs

Valentina Penza https://orcid.org/0000-0002-3948-2268
Luca Bertello https://orcid.org/0000-0002-1155-7141
Matteo Cantoresi https://orcid.org/0000-0003-4898-2683
Serena Criscuoli https://orcid.org/0000-0002-4525-9038
Lorenza Lucaferri https://orcid.org/0009-0000-9757-8455
Raffaele Reda https://orcid.org/0000-0001-8623-5318
Simone Ulzega https://orcid.org/0000-0002-8744-4266
Francesco Berrilli https://orcid.org/0000-0002-2276-3733

References

Abduallah, Y., Wang, J. T. L., Shen, Y., et al. 2021, arXiv:2107.11042
Abreu, J. A., Beer, J., Steinhilber, F., Tobias, S. M., & Weiss, N. O. 2008, GeoRL, 35, L20109
Arlt, R., & Vaquero, J. M. 2020, LRSP, 17, 1
Ball, W. T., Krivova, N. A., Unruh, Y. C., Haigh, J. D., & Solanki, S. K. 2014, JAtS, 71, 4086
Bazilevskaya, G., Broomhall, A. M., Elsworth, Y., & Nakariakov, V. M. 2014, SSRv, 186, 359
Berrilli, F., Criscuoli, S., Penza, V., & Lovric, M. 2020, SoPh, 295, 38
Berrilli, F., Ermolli, I., Florio, A., & Pietropaolo, E. 1999, A&A, 344, 965
Bordi, I., Berrilli, F., & Pietropaolo, E. 2015, AnGeo, 33, 267
Brehm, N., Bayliss, A., Christl, M., et al. 2021, NatGe, 14, 10

Caballero-Lopez, R. A., & Moraal, H. 2004, JGRA, 109, A01101
Chapman, G. A., Cookson, A. M., & Dobias, J. J. 1994, ApJ, 423, 403
Chapman, G. A., Cookson, A. M., & Dobias, J. J. 1997, ApJ, 482, 541
Chapman, G. A., Dobias, J. J., & Arias, T. 2011, ApJ, 728, 150
Chatzistergos, T., Ermolli, I., Krivova, N. A., & K., S. S. 2019, A&A, 625, A69
Chatzistergos, T., Ermolli, I., Krivova, N. A., et al. 2020, A&A, 639, A88
Chatzistergos, T., Ermolli, I., Krivova, N. A., et al. 2022, A&A, 667, A167
Chatzistergos, T., Krivova, N. A., & Y., K. K. 2023, JASTP, 252, 106150
Chatzistergos, T., Krivova, N. A., & Y., K. K. 2024, SoPh, 299, 21
Coddington, O., Lean, J. L., Pilewskie, P., Snow, M., & Lindholm, D. 2016, BAMS, 97, 1265
Criscuoli, S., Penza, V., Lovric, M., & Berrilli, F. 2018, ApJ, 865, 22
Devil, P., Singh, J., Chandra, R., Priyal, M., & Josh, R. 2021, SoPh, 296, 49
Ermolli, I., Berrilli, F., & Florio, A. 2003, A&A, 412, 857
Ermolli, I., Criscuoli, S., & Giorgi, F. 2011, CoSka, 41, 73
Egorova, T., Schmutz, W., Rozanov, E., et al. 2018, A&A, 615, A85
Faurobert, M. 2019, in The Sun as a Guide to Stellar Physics, ed. O. Engvold, J.-C. Vial, & A. Skumanich (Amsterdam: Elsevier), 267
Fontenla, J. M., Harder, J., Livingston, W., Snow, M., & Woods, T. 2011, JGRD, 116, D20108
Foukal, P., Bernasconi, P., Eaton, H., & Rust, D. 2004, ApJL, 611, L57
Foukal, P., & Lean, J. 1988, ApJ, 328, 347
Galuzzo, D., Cagnazzo, C., Berrilli, F., Fierli, F., & Giovannelli, L. 2021, ApJ, 909, 191
Gleeson, L. J., & Axford, W. I. 1968, ApJ, 154, 1011
Gleissberg, W. 1939, Obs, 62, 158
Gnevyshev, M., & Ohl, A. 1948, Astron. Zh, 25, 18
Gnevyshev, M. N. 1967, SoPh, 1, 107
Hale, G. E., Ellerman, F., Nicholson, S. B., & Joy, A. H. 1919, ApJ, 49, 153
Huang, N. E., Shen, Z., Long, S. R., et al. 1998, RSPSA, 454, 903
Intergovernmental Panel on Climate Change (IPCC) 2023, Climate Change 2021—The Physical Science Basis: Working Group I Contribution to the Sixth Assessment Report of the Intergovernmental Panel on Climate Change (Cambridge: Cambridge Univ. Press)
Jefferies, S. M., Fleck, B., Murphy, N., & Berrilli, F. 2019, ApJL, 884, L8
Jungclaus, J. H., Bard, E., Baroni, M., et al. 2017, GMD, 10, 4005
Kolotkov, D. Y., Broomhall, A. M., & Nakariakov, V. M. 2015a, MNRAS, 451, 4360
Kolotkov, D. Y., Nakariakov, V. M., Kupriyanova, E. G., Ratcliffe, H., & Shibasaki, K. 2015b, A&A, 574, A53
Kopp, G., Krivova, N., Wu, C. J., & Lean, J. 2016, SoPh, 291, 2951
Kopp, G., & Shapiro, A. 2021, SoPh, 296, 60
Kren, A. C., Pilewskie, P., & Coddington, O. 2017, JSWSC, 7, A10
Lean, J., Beer, J., & Bradley, R. 1995, GeoRL, 22, 3195
Lean, J. L. 2018, E&SS, 5, 133
Lean, J. L., Coddington, O., Marchenko, S. V., et al. 2020, E&SS, 7, 00645
L'Ecuyer, T. S., Beaudoing, H. K., Rodell, M., et al. 2015, JCli, 28, 8319
Li, Q., Wu, J., Xu, Z.-w., & Wu, J. 2007, ChA&A, 31, 261
Linsky, J. L. 2017, ARA&A, 55, 159
Liu, H.-L., Rempel, M., Danabasoglu, G., Solomon, S. C., & McInerney, J. M. 2023, JGRD, 128, e2022JD037626
Lockwood, M. 2012, SGeo, 33, 503
Lockwood, M., & Ball, W. T. 2020, RSPSA, 476, 20200077
Lovric, M., Tosone, F., Pietropaolo, E., et al. 2017, JSWSC, 7, A6
Mandal, S., Krivova, N. A., Solanki, S. K., Sinha, N., & Banerjee, D. 2020, A&A, 640, A78
Marchenko, S., Lean, J., & DeLand, M. T. 2022, A&A, 936, 158
Matthes, K., Funke, B., Andersson, M. E., et al. 2017, GMD, 10, 2247
McCracken, K., & Beer, J. 2007, JGRA, 112, A10101
Modi, A., Estrela, R., & Valio, A. 2023, MNRAS, 525, 5168
Montillet, J., Finsterle, W., Kermarrec, G., et al. 2022, JGRD, 127, e2021JD036146
Muscheler, R., Adolphi, F., Herbst, K., & Nilsson, A. 2016, SoPh, 291, 3025
Muscheler, R., Joos, F., Beer, J., et al. 2007, QSRv, 26, 82
Nakariakov, V. M., Inglis, A. R., Zimovets, I. V., et al. 2010, PPCF, 52, 124009
Oster, L., Schatten, K. H., & Sofia, S. 1982, ApJ, 256, 768
Owens, M. J., Lockwood, M., Riley, P., & Linker, J. 2017, JGRA, 122, 980
Penza, V., Berrilli, F., Bertello, L., Cantoresi, M., & Criscuoli, S. 2021, ApJL, 922, L12
Penza, V., Berrilli, F., Bertello, L., et al. 2022, ApJ, 937, 84
Penza, V., Caccin, B., Ermolli, I., Centrone, M., & Gomez, M. T. 2003, in Solar Variability as an Input to the Earth's Environment, ed. A. Wilson, Vol. 535 (Noordwijk: ESA), 299
Petrie, G., Criscuoli, S., & Bertello, L. 2021, in Solar Physics and Solar Wind, ed. N. E. Raouafi et al. Vol. 1 (New York: Wiley), 83
Preminger, D. G., & Walton, S. R. 2006, SoPh, 235, 387
Rackham, B. V., Espinoza, N., Berdyugina, S. V., et al. 2023, RASTI, 2, 148
Reda, R., Stumpo, M., Giovannelli, L., Alberti, T., & Consolini, G. 2024, RLSFN, 35, 305
Rilling, G., Flandrin, P., & Gonçalves, P. 2003, in Proc. IEEE-EURASIP Workshop on Nonlinear Signal and Image Processing (NSIP-03) (Piscataway, NJ: IEEE), 3
Schwabe, H., & Schwabe, H. 1844, AN, 21, 233
Shapiro, A. I., Schmutz, W., Rozanov, E., et al. 2011, A&A, 529, A67
Simpson, J. A. 2000, SSRv, 93, 11
Skumanich, A., Lean, J., Livingston, W., & White, O. 1984, AJ, 282, 776
Sofia, S., Oster, L., & Schatten, K. 1982, SoPh, 80, 87
Solanki, S. K., & Fligge, M. 1999, GeoRL, 26, 2465
Solanki, S. K., Krivova, N. A., & Haigh, J. D. 2013, ARA&A, 51, 311
Stangalini, M., Consolini, G., Berrilli, F., De Michelis, P., & Tozzi, R. 2014, A&A, 569, A102
Steinegger, M., Brandt, P. N., & Haupt, H. F. 1996, A&A, 310, 635
Steinhilber, F., Abreu, J., Beer, J., & McCracken, K. 2010, JGRA, 115, A01104
Steinhilber, F., Abreu, J. A., Beer, J., et al. 2012, PNAS, 109, 5967
Steinhilber, F., Beer, J., & Fröhlich, C. 2009, GeoRL, 36, L19704
Stuiver, M., & Braziunas, T. F. 1998, GeoRL, 25, 329
Suess, H. E. 1980, Radiocarbon, 22, 200
Tapping, K. F., Boteler, D., Charbonneau, P., et al. 2007, SoPh, 246, 309
Terradas, J., Oliver, R., & Ballester, J. L. 2004, ApJ, 614, 435
Usoskin, I. G. 2017, LRSP, 14, 3
Usoskin, I. G., A., G., Kovaltsov, G., Mishev, A., & Mikhailov, V. 2017, JGRA, 122, 3875
Usoskin, I. G., Alanko-Huotari, K., Kovaltsov, G. A., & Mursula, K. 2005, JGRA, 110, A12108
Usoskin, I. G., Solanki, S., Krivova, N., et al. 2021, A&A, 649, A141
Usoskin, I. G., Solanki, S. K., & Kovaltsov, G. A. 2007, A&A, 471, 301
Vecchio, A., Lepreti, F., Laurenza, M., Alberti, T., & Carbone, V. 2017, A&A, 599, A58
Vecchio, A., Lepreti, F., Laurenza, M., Carbone, V., & Alberti, T. 2019, NCimC, 42, 15
Volobuev, D. 2009, SoPh, 258, 319
Vonmoos, M., Beer, J., & Muscheler, R. 2006, JGRA, 111, A10105
Walton, S. R., Preminger, D. G., & Chapman, G. 2003, SoPh, 203, 301W
Wang, Y. M., & Lean, J. L. 2021, ApJ, 920, 100
Wang, Y. M., Lean, J. L., & Sheeley, N. R. J. 2005, ApJ, 625, 522
Willson, R. C., Gulkis, S., Janssen, M., Hudson, H. S., & Chapman, G. A. 1981, Sci, 211, 700
Wu, C.-J., Krivova, N. A., Solanki, S. K., & Usoskin, I. G. 2018, A&A, 620, A120
Yeo, K. L., Krivova, N. A., & Solanki, S. K. 2014, SSRv, 186, 137
Yeo, K. L., Krivova, N. A., & Solanki, S. K. 2017a, JGRA, 122, 3888
Yeo, K. L., Solanki, S. K., Krivova, N. A., et al. 2020, GeoRL, 47, e90243
Yeo, K. L., Solanki, S. K., Norris, C. M., et al. 2017b, PhRvL, 119, 091102